PROCEEDINGS, 42nd Workshop on Geothermal Reservoir Engineering
Stanford University, Stanford, California, February 13-15, 2017

Enhanced Characterization of Induced Seismicity

Gregory A. Newman and Peter V. Petrov

Lawrence Berkeley National Laboratory, Earth Sciences Division, CA, USA

Corresponding author: gnewman@lbl.gov

Keywords: Seismic moment tensor; 3-D inversion; Raft River Geothermal Field

ABSTRACT

At the most geothermal fields the activities associated with geothermal energy production and or enhanced geothermal system (EGS) development will cause increase seismicity, where the physical mechanisms are still not fully understood. For the definition of the nature of induced seismicity, a second-order dynamic moment tensor analysis may be used to ascertain if seismicity is arising from stress release along preexisting faults or from fracture permeability creation associated with EGS activities. With dynamic moment tensor analysis an accurate estimation of the source parameters, including location, in the presence of complex geological media with highly variable seismic velocity properties is a non-trivial task. Here, we employ the full elastic waveform inversion (FWI) in Laplace-Fourier domain to estimate the location and seismic moment tensor parameters of sources embedded in 3D isotropic heterogeneous media. Forward modeling is carried out with a 3D finite-difference code that generates P- and S-waves from the point sources defined by second-order moment tensors. The inversion algorithm is based on nonlinear gradient calculations for the minimization of the objective function for event location and source moment updating based upon the linear least-squares normal equations for the micro-seismic event at an assumed location, embedded in complex heterogeneous geological media. The FWI algorithm is shown to be stable in the presence of complex geometry including faults and random Gaussian noise. We present results of testing the FWI methodology on the synthetic dataset for the Raft River geothermal field, Idaho. The detectors were placed on the earth surface and seismic events were simulated at the depth about 2000 meters. Matching the waveforms from seismic events provides improved source location along with estimates of the pertinent components of the moment tensor. Investigation of the influence of velocity model and an initial position of an event are performed.

1. RAFT RIVER GEOTHERMAL AREA

Better understanding the physical mechanisms of induced seismicity associated with geothermal systems is currently of great interest with the development of enhanced geothermal systems (EGS) energy production. The Raft River geothermal field is a Department of Energy EGS test site, located in Cassia county Idaho roughly 100 miles northwest of Salt Lake City on the Utah-Idaho border. The wells at Raft River encountered 5,000 ft. of Quaternary and Tertiary volcanic and volcanoclastic rocks before their completion in the Precambrian basement. The Elba quartzite, located in Precambrian rocks, is the primary geothermal reservoir with an average resource temperature of 300 °F(Ayling et al., 2011; Jones et al., 2011). Analysis of water chemistry indicates that the field is bisected into two regions separated by shear faulting, termed the Narrows Zone (Figure 1a), as described by Ayling & Moore (2013). The Narrows Zone strikes to the northeast through the middle of the field. Microseismic activity attributed to plant activity suggest that while acting as a barrier between the two regions, the Narrows zone allows for fluid movement along its length. The rocks in Precambrian basement have very low porosities, and fluid flow in the system is highly dependent on fracture conductivity. Temperature and microseismic data suggest that fluid injected into well RRG-9 ST1 passes through the intersecting fracture zone, connecting into the Narrows Zone, and then moves along its length to the northeast. Tracking production and distribution of geothermal fluids is realized with the microseismic monitoring which include definition of seismic source location and mechanisms. Essentially that knowledge of seismic-source mechanisms can provide insights into the fracturing behavior of the reservoir and surrounding rocks and an understanding of the evolution of the stress field. On the Raft River geothermal field seismic monitoring is performed with the 8 stations (Figure 1b).

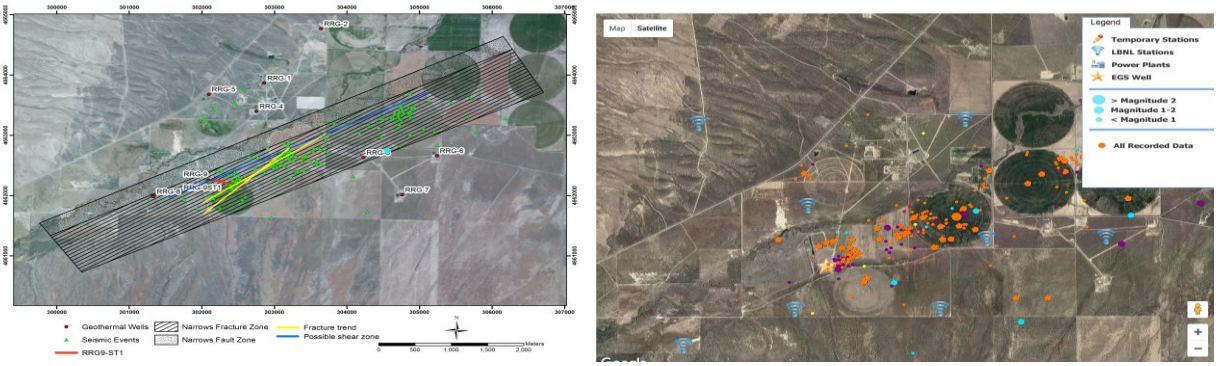

a) b)

Figure 1: (a) Well Locations Relative to Narrows Structure in Raft River Geothermal Area (b) Geometry of survey and locations of micro-earthquakes.

2. METHODOLOGY

The objective is to determine the best fitting source-moment model that might arise from fluid-related processes in the geothermal system. Here we try to address this problem from the standpoint of full-waveform inversion (FWI) (Plessix et al.2010 and Sirgue et al.2010). We propose a full-waveform approach for the earthquake source model using data in Laplace-Fourier domain from a few monitoring surface stations. Waveform inversion is a nonlinear optimization technique that uses full wavefield propagation for simulating data and iteratively matches seismic waveforms to estimate model parameters. One of the advantages of FWI is the possibility to invert multicomponent data consistently. The algorithm is based on nonlinear gradient calculations for the minimization of the objective function for event location and source moment updating based upon the linear least-squares normal equations for a micro-seismic source embedded in complex heterogeneous geological media.

Following the inverse problem formulation in the Laplace-Fourier domain we solve this nonlinear problem by minimizing the error functional in the L_2 norm

$$\phi(\mathbf{m},\mathbf{r}_s)=\sum_{s_k}\sum_{q}\frac{1}{2}\left(\mathbf{d}_q^{obs}(s_k)-\mathbf{d}_{q,k}^{sim}\right)^H\mathbf{E}^H\mathbf{E}\left(\mathbf{d}_q^{obs}(s_k)-\mathbf{d}_{q,k}^{sim}\right) \tag{1}$$

In eq. (1) $\mathbf{d}_q^{obs}(s_k),\mathbf{d}_{q,k}^{sim}$ are the observed and predicted data vectors, with subscript q indicating the station position, $\mathbf{E}$ - the diagonal matrix of weights defined by the data error, and symbols "H, T"- the Hermitian conjugate and transpose operations respectively. The observed data vectors consist of the Laplace-Fourier image of elastic displacement velocities, obtained from the measured time-domain seismic wavefield data with a set of complex frequencies $s_k=\sigma_k+i\omega_k, k=1...N_k$, where σ_k is the Laplace damping constant and ω_k is the angular frequency with $i=\sqrt{-1}$:

$$\mathbf{d}_q^{obs}(s_k)=\int_0^\infty\mathbf{d}_q^{obs}(t)e^{-s_kt}dt \tag{2}$$

Predicted data $\mathbf{d}_{q,k}^{sim}$ are defined by the displacement velocity field and depend upon the velocity model and source model

$$\mathbf{d}_{q,k}^{sim}=\hat{\mathbf{Q}}_q\mathbf{v}_k, \tag{3}$$

where $\hat{\mathbf{Q}}_q$ is an interpolation operator applied to the calculated velocity field in the vicinity of the station. For the elastic medium with density ρ, bulk and shear moduli κ,μ, the velocity components $\mathbf{v}_k=\left(v_x^k,v_y^k,v_z^k\right)$ specified in eq. (3), satisfy the equations of motion, which may be directly obtained taking the Laplace-Fourier transform of the time-domain system for complex frequency s_k. After finite-difference implementation, specifically for velocity and stress formulation (Virieux 1986), a linear system is given by:

$$\begin{aligned}&\mathbf{K}_k\mathbf{v}_k=s_k\langle\mathbf{b}\rangle\hat{\mathbf{D}}_\tau\mathbf{M}_k(\mathbf{r}),\ \mathbf{K}_k=\left(s_k^2\mathbf{I}-\langle\mathbf{b}\rangle\hat{\mathbf{D}}_\tau\langle\mathbf{k\mu}\rangle\hat{\mathbf{D}}_v\right)\\&\mathbf{M}_k=\left(M_{xx},M_{xy},M_{xz},M_{yy},M_{yz},M_{zz}\right)^T\end{aligned}, \tag{4}$$

where $\mathbf{M}$ is the Laplace-Fourier image of spatiotemporal moment density, $\langle \mathbf{k\mu} \rangle, \langle \mathbf{b} \rangle$ are block matrices of the averaged elastic parameters and $\hat{\mathbf{D}}_\tau, \hat{\mathbf{D}}_v$ are the finite-difference operators, which explicit expression can be found in (Petrov, Newman 2012, 2014).

The formal solution of (4) can be written via a Green function $\mathbf{G}_k$ as

$$\mathbf{v}_k = \mathbf{G}_k \mathbf{M}_k, \ \mathbf{G}_k = s_k \ \mathbf{K}_k^{-1} \langle \mathbf{b} \rangle \hat{\mathbf{D}}_\tau \tag{5}$$

When the source-receiver distance is much larger than the source scale and the wavelength, the seismic source can be considered as the point source with the position $\mathbf{r}_s = (x_s, y_s, z_s)$ and represented by its moment tensor (Aki and Richards, 2002)

$$\mathbf{m}_k = \left(m_{xx}^k, m_{xy}^k, m_{xz}^k, m_{yy}^k, m_{yz}^k, m_{zz}^k\right)^T \delta(\mathbf{r}_s - \mathbf{r}), \ \mathbf{m}_k = \int_V \mathbf{M}_k(s_k, \mathbf{r}) dV \tag{6}$$

Then equation (5) and, accordingly, the vector of predicted data $\mathbf{d}_k^{sim} = \left(d_{1,k}^{sim}, d_{2,k}^{sim}, d_{2,k}^{sim} ... d_{q,k}^{sim}\right)$ transforms to

$$\mathbf{v}_k = \mathbf{G}_k \mathbf{P} \mathbf{m}_k, \ \mathbf{d}_k^{sim} = \mathbf{B}_k \mathbf{m}_k, \quad \mathbf{B}_k = \mathbf{Q} \mathbf{G}_k \mathbf{P}, \tag{7}$$

where operator $\mathbf{P} = diag\left(\delta(\mathbf{r} - \mathbf{r}_s), \delta(\mathbf{r} - \mathbf{r}_s), \delta(\mathbf{r} - \mathbf{r}_s), \delta(\mathbf{r} - \mathbf{r}_s), \delta(\mathbf{r} - \mathbf{r}_s), \delta(\mathbf{r} - \mathbf{r}_s)\right)$ defines the source position for each component of moment tensor.

To carry out simultaneous inversion for $\mathbf{r}_s$ and $\mathbf{m}(s_k)$ we employ an iterative scheme, where each iteration is divided into two steps. At first we suppose the known the position of the source at point $\mathbf{r}_s^0$ and define the best fit for the moment tensor. Because of the known position of the source the minimization of (1) becomes a linear problem relative to the 6 components of the moment tensor and can be defined by the least square method from the normalized equation (Johnoson L.R., 2014,)

$$\mathbf{B}_k \left(\mathbf{r}_s^0\right)^H \mathbf{E}^H \mathbf{E} \left(\mathbf{d}_k^{obs} - \mathbf{B}_k \left(\mathbf{r}_s^0\right) \cdot \mathbf{m}_k^0\right) = 0, \tag{8}$$

Elements of sensitivity matrix $\mathbf{B}_k \left(\mathbf{r}_s^0\right)$ are estimated from the 6 solutions of forward problem(4), separately for each tensor component. Specifically

$$\mathbf{B}_k = \left[\mathbf{b}^1, \mathbf{b}^2, ..., \mathbf{b}^6\right], \mathbf{b}^l = \mathbf{B}_k \cdot \mathbf{e}_l = \mathbf{Q} \mathbf{G}_k \mathbf{P} \cdot \mathbf{e}_l, \ l = 1...6 \tag{9}$$

where $\mathbf{e}_l$ is a 6 component vector with the one in the l -position and zeros in the others.

At the second step we update the source position using NLCG method (Polyak & Ribiere 1969) and difference between observed and predicted data given by $\mathbf{e}_k^0 = \left(\mathbf{d}_k^{obs}(s_k) - \mathbf{d}_k^{sim,0}\right)$, where $\mathbf{d}_k^{sim,0} = \mathbf{B}_k \left(\mathbf{r}_s^0\right) \mathbf{m}_k^0$ is obtained at the first step for the fixed source position $\mathbf{r}_s^0$:

$$\mathbf{r}_s^1 = \mathbf{r}_s^0 + \alpha \frac{\partial \phi}{\partial \mathbf{r}_s}, \ \frac{\partial \phi}{\partial \mathbf{r}_s} = -2 \mathrm{Re}\left(\left(\mathbf{e}_k^0 \mathbf{E}\right)^H \mathbf{E} \frac{\partial \mathbf{d}_k^{sim,0}}{\partial \mathbf{r}_s}\right) = -2 \mathrm{Re}\left(\left(\mathbf{e}_k^0 \mathbf{E}\right)^H \mathbf{E} \cdot \mathbf{Q} \mathbf{G}_k \frac{\partial \mathbf{P}}{\partial \mathbf{r}_s} \mathbf{m}_k^0\right) = -2 \mathrm{Re}\left(\mathbf{g}^H \cdot s_k \langle \mathbf{b} \rangle \hat{\mathbf{D}}_\tau \frac{\partial}{\partial \mathbf{r}_s} \mathbf{P}\left(\mathbf{r}_s^0\right) \mathbf{m}_k^0\right). \tag{10}$$

Here vector $\mathbf{g}^H$ can be obtained from the solution of the adjoint equation (symbol "*" is the conjugate operation)

$$\mathbf{K}_k^T \mathbf{g}^* = \mathbf{Q}^T \mathbf{E} \mathbf{E}^H \left(\mathbf{d}_k^{obs}(s_k) - \mathbf{d}_k^{sim,0}\right)^* \tag{11}$$

The iteration process repeats until the relative gradient changes become less than 0.5%.

3. RAFT RIVER 3-D ELASTIC MODEL

For the algorithm validation we use the part of 3D Raft River velocity model designed by Nash and Moore (2012). To reduce both the required memory and computing time, we used a part of the model, which contains all eight LBNL seismic stations. The model is rotated so that Narrows Zone aligns along the X-axis with a broadside extension of $396 \le x \le 5724, 1068 \le y \le 5148$ (in meters). The depth extend of the model is $0 \le z \le 2256$ (in meters). The distribution of P-wave velocities in the planes $x = 3600$ and $z = 2000$ m are shown in Figures 2. The number of grid nodes is $111 \times 85 \times 47$ with the grid spacing of 48 m. A free surface boundary condition was imposed on the surface z=0. On the other boundaries the perfectly match layer (PML) boundary condition is applied, with 5 cells in each direction.

Synthetic data were generated by the Laplace-Fourier domain finite-difference modeling technique (Petrov and Newman 2012) with the same grid size. Each of 8 seismic station records three components of velocity displacement near the surface. The projections of survey geometry are presented in Figure 2. Two different positions of microseismic sources were examined near the Narrows zone at $x_s = 4000, y_s = 3600, z_s = 1800$ and $x_s = 4500, y_s = 2000, z_s = 1500$ meters. The value of the moment tensor was the same in both cases and included all 6 components. During the inversion all three components of velocity displacement were used as the observed data from all stations.

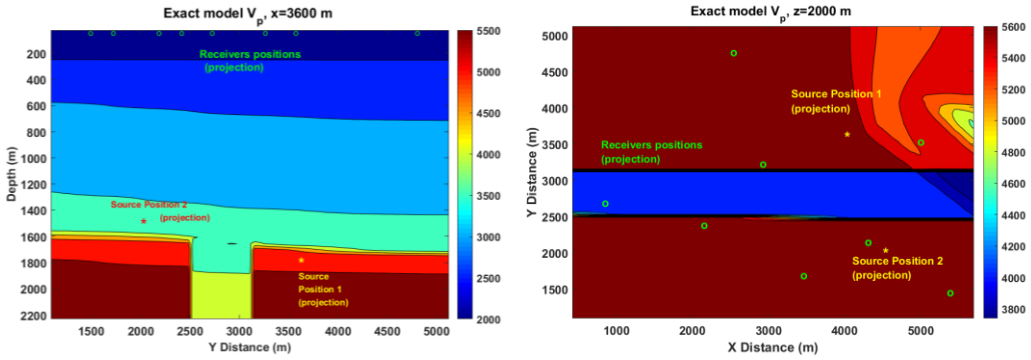

Figure 2: P-wave velocities (m/s) of the Raft River elastic model and seismic survey geometry

5. INVERSE MODELING RESULTS

For the inversion we used only one complex frequency with f =2 Hz and damping constant $\sigma = 6$ 1/s. The initial positions of the seismic sources were selected at a distance of 300…500 meters from the exact location. As Figures 3 show, the inversion gives correct results for the location of the source and does not depend on the initial position of source inside the convergence radius, which is at least 500 meters.

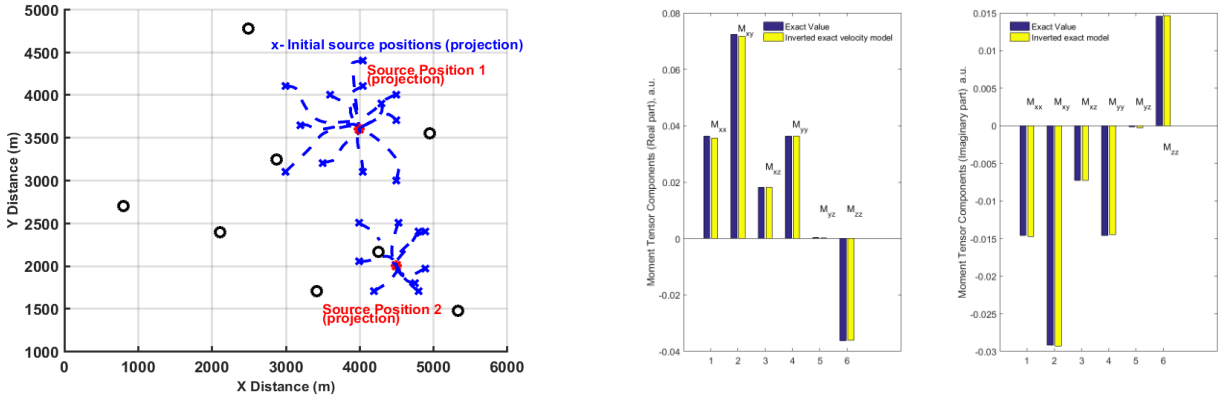

a) b)

Figure 3: The trajectories of inversion steps during the source position definitions (a) and inverted moment tensor for the exact velocity model (b).

To investigate sensitivity of results to the velocity model we performed inversions with a few inexact models, which were obtained by the different levels of smoothing the exact velocity distribution (Figure 4). The difference between models may be characterized by the relative error:

$$e_s = \left\| V_{p,s}^{exact} - V_{p,s}^{smooth} \right\| / \left\| V_{p,s}^{exact} \right\| * 100\% \qquad (12)$$

The inversions were performed for the source in position 1. Despite the difference between exact and used models the errors in the estimated source coordinates (Figure 5a) are relatively small in contrast with the moment-tensor elements (Figure 5b), which are more sensitive to the velocity model used in FWI. Increasing errors e_s in the velocity model leads to the corresponding errors in the moment tensor estimates, although relations between different components are still approximately conserved. If the relative error for the moment tensor is defined as

$$e_M = \left\| M_i^{exact} - M_i^{inv} \right\| / \left\| M_i^{exact} \right\| * 100\% \qquad (13)$$

then we can obtain connection between e_s and e_M as shown in Figure 5b.

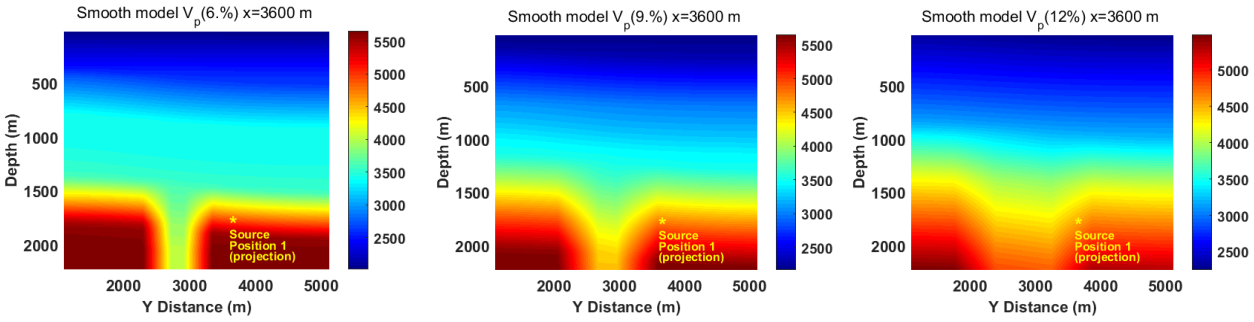

a) b) c)

Figure 4: Inexact velocity models with the different levels deviation (smoothing) from the exact model (12) a) $e_s = 6\%$**, b)** $e_s = 9\%$**, c)** $e_s = 12\%$**.**

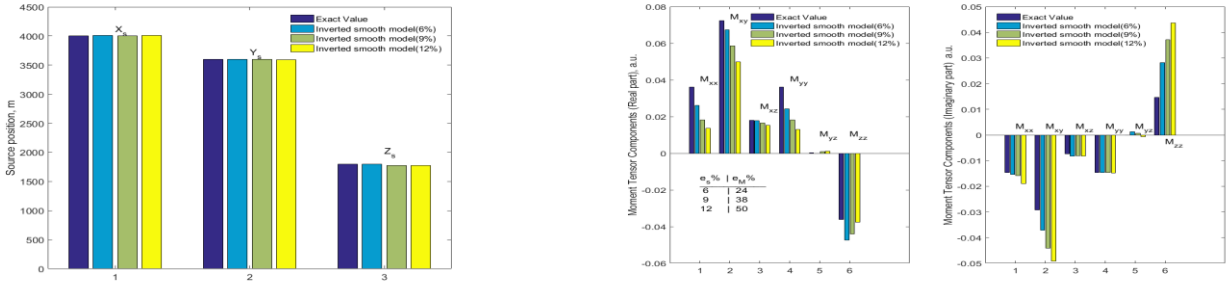

a) b)

Figure 5: Results of inversion the source position (a) and moment tensor for different inexact velocity models with the relative deviation error (12) $e_s = 6\%, 9\%, 12\%$ **(b).**

It is also important to evaluate the influence of noise in the input data on the inversion results. We add random Gaussian noise in the Laplace-Fourier image of the observed data with the variance equal to 5 and 10%. The inversion algorithm, applied together with the exact velocity model estimates correct values of $\mathbf{r}_s$ and $\mathbf{m}$. For both values of noise, the errors in the estimated source coordinates are small (Figure 6a), whereas the moment-tensor elements are more sensitive to the magnitude of the noise (Figure 6b,c).

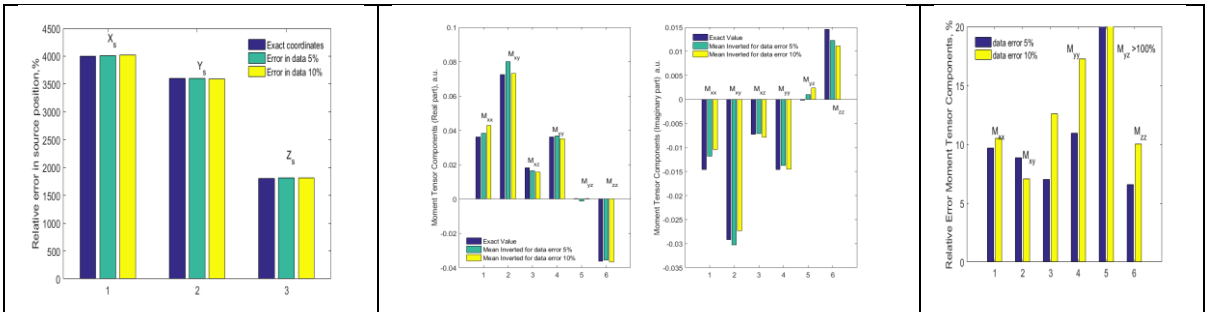

a) b) c)

Figure 6: Results of inversion with the random noise the source position (a) mean values (b) and relative error (c) of moment tensor components.

6. DISCUSSION

Comparing FWI results with the inversion of the moment tensor based on the different analytic representations of the Green function is beneficial in investigating seismic events in complex 3D heterogeneous media, which are very different from homogeneous or layered

media. Our simulations show high sensitivity of the moment tensor components inversion to the velocity model, which may be critical for understanding physical processes if the structure of micro-seismic sources is considered as a marker of fluid-related processes in the geothermal system. By now FWI may be the only way to provide properly 3D complex geological structures in the inversion of moment tensor components and it may be an indicator for utility and accuracy of any other approximate approaches. As the result of this approach we obtained Laplace-Fourier image of moment tensor and after inverse transformation it may be possible to define the dynamic moment tensor.

The method presented here requests an initial approximation of source location, but we should take into account that deviation from the exact location may be up to 1 km. Moreover it may be easily obtain an initial estimate of the source location by other methods, for example based on a travel time techniques. The inverted source position may be different for different frequencies that theoretically allowing a possibility of tracking the changes in the source mechanism and position during a micro-earthquake event in time and estimating its volume.

Obviously the FWI problem is a large computational expense, but the development of parallel direct methods for the solution of 3D elastic forward problems can essentially reduce the time to solution for such problems.

7. CONCLUSION

We presented a FWI method for estimation of micro-seismic sources parameters (location and moment tensor) in Laplace-Fourier domain for 3D elastic heterogeneous media. The stability of the algorithm was tested for the input data contaminated with Gaussian noise and inexact velocity models. In noise-free tests the method converges to the exact values of the source parameters. The inversion provides very good source location estimates and reasonable approximate values of moment tensor components in the presence of noise and velocity model deviation. The methodology was tested on a synthetic data set generated for Raft River geothermal field.

8. ACKNOWLEDGEMENTS

This material is based upon work supported by the U.S. Department of Energy Office of Energy Efficiency and Renewable Energy (EERE) Geothermal Technologies Program, under Award Number GT-480010-19823-10. Computational resources were provided by the National Energy Research Scientific Computing (NERSC) Center. All simulations were performed on the CRAY XC30 supercomputers. The authors acknowledge Joseph Moore, John Queen for providing the 3D elastic Raft River model.

9. REFERENCES

Aki, K., and P. G. Richards, 2002, Quantitative seismology:University Science Books.

Ayling B., P. Molling, R. Nye and J. Moore, 2011, Fluid geochemistry at the Raft River geothermal field, Idaho: new data and hydrogeological implications: Proceedings, 36thWorkshop on Geothermal Reservoir Engineering, SGP-TR-191

Ayling, B., & Moore, J. N. (2013). Fluid geochemistry at the Raft River geothermal field, Idaho, USA: New data and hydrogeological implications. Geothermics, 116-126.

Jones C., J. Moore, W. Teplow and S. Craig, 2011, Geology and hydrothermal alteration of the Raft River geothermal system, Idaho: Proceedings, 36th Workshop on Geothermal Reservoir Engineering, SGP-TR-191

Johnoson L.R., 2014, Source Mechanisms of Induced Earthquakes at The Geysers Geothermal Reservoir Pure Appl. Geophys. 171, 1641–1668

Nash, G. D., and Moore, J. N., 2012, “Raft River EGS Project: A GIS-Centric Review of Geology”, GRC Transactions, 36, 951 - 958.

Polyak E., and Ribi`ere G., 1969. Note sur la convergence desm´ethods conjug´ ees, Rev. Fr. Inr. Rech. Oper. 16, 35–43.

Petrov, P.V., Newman, G. A., 2012. 3D finite-difference modeling of elastic wave propagation in the Laplace-Fourier domain, Geophysics, 77, T137-T155.

Petrov P.V., Newman G. A., 2014. Three-dimensional inverse modelling of damped elastic wave propagation in the Fourier domain. Geophysical Journal International 198, 1599–1617

Plessix R. E., Baeten G., de Maag J. W., Klaasen M., Rujie Z. and Zhifei T. 2010. Application of acoustic full-waveform inversion to a low-frequency large-offset land data set: 80th Annual International Meeting, SEG, Expanded Abstracts, 930–934

Sirgue L., Barkved O.I., Dellinger J., Etgen J., Albertin U. and Kommedal J.H. 2010. Full waveform inversion: the next leap forward in imaging at Valhall. First Break 28, 65–70.

Virieux, J., 1986, P-SV wave propagation in heterogeneous media: Velocity-stress finite-difference method, Geophysics **51**, 889–901.